Turkish Journal of Earth Sciences

Volume 33 | Number 4 Article 5

5-27-2024

Stochastic 1-D reactive transport simulations to assess silica and carbonate phases during the CO2 reinjection process in metasediments

SELÇUK EROL
Department of Energy Systems Engineering, Faculty of Engineering, İzmir Institute of Technology, İzmir, Turkiye

Follow this and additional works at: https://journals.tubitak.gov.tr/earth

 Part of the Earth Sciences Commons

Recommended Citation

EROL, SELÇUK (2024) "Stochastic 1-D reactive transport simulations to assess silica and carbonate phases during the CO2 reinjection process in metasediments," *Turkish Journal of Earth Sciences*: Vol. 33: No. 4, Article 5. https://doi.org/10.55730/1300-0985.1922
Available at: https://journals.tubitak.gov.tr/earth/vol33/iss4/5



This work is licensed under a Creative Commons Attribution 4.0 International License.
This Research Article is brought to you for free and open access by TÜBİTAK Academic Journals. It has been accepted for inclusion in Turkish Journal of Earth Sciences by an authorized editor of TÜBİTAK Academic Journals. For more information, please contact academic.publications@tubitak.gov.tr

TÜBİTAK

Turkish Journal of Earth Sciences

http://journals.tubitak.gov.tr/earth/

Research Article

Turkish J Earth Sci
(2024) 33: 441-456
© TÜBİTAK
doi:10.55730/1300-0985.1922

Stochastic 1-D reactive transport simulations to assess silica and carbonate phases during the CO_2 reinjection process in metasediments

Selçuk EROL*
[1]Department of Energy Systems Engineering, Faculty of Engineering, İzmir Institute of Technology, İzmir, Turkiye

Received: 20.09.2023 • **Accepted/Published Online:** 21.03.2024 • **Final Version:** 27.05.2024

Abstract: One proposed method to mitigate carbon emission is to mineralize the CO_2 in deep geothermal reservoirs while mixing the coproduced CO_2 with the effluent fluid for reinjection. The injection fluid temperature fluctuates due to the mixing process between CO_2-charged water and the effluent fluid, and compressor interruptions change the thermodynamic conditions that influence the fluid-rock interaction in the reservoir. Mineral dissolution or precipitations are associated with changes in permeability and porosity that affect the flow and, eventually, the lifespan of the reservoir. A combined stochastic–reactive transport simulation approach is useful for inspection purposes. Moreover, the stochastic algorithm validates the deterministic reactive transport simulation and demonstrates the time evolution of a chemically reacting system in the reservoir. This study examines a range of injection temperatures between 80 °C and 120 °C to evaluate silica and calcite precipitation along a flow path. One-dimensional (1-D) reactive transport and compartment-based stochastic reaction-diffusion-advection Gillespie algorithms are carried out. The 1-D model represents a reservoir feed zone of around 2300 m. Two common metasediment rock types are evaluated for inspection. The first one is the muscovite schist, which has approximately 60% quartz, and the second is the quartz schist, consisting of roughly 90% quartz. The stochastic method can be applied more effectively if the chemical system is completely defined with proper reaction rates as a function of temperature. The mixing ratio of the coproduced CO_2 over the effluent fluid is around 0.0028. Simulation results show that CO_2 is partially sequestrated as calcite within the first 10 m of the entrance to the reservoir and plugs the pores completely in the muscovite schist scenario. Chalcedony and α-cristobalite precipitate as secondary minerals evenly along the flow path. CO_2 injection into a quartz schist layer is more appropriate for geochemical interactions below 120 °C.

Key words: Stochastic, Gillespie, reactive transport, CO_2 injection, metasediment

1. Introduction

One of the adversities of power utilization in geothermal power plants is significant emissions of noncondensable gases (NCG), mainly consisting of CO_2. According to Fridriksson et al. (2017), the average global CO_2 emission factor of geothermal power production is around 122 g/kWh. Turkish geothermal production causes approximately ten times higher CO_2 emissions than the worldwide average (Akın et al., 2020).

An effective way to diminish CO_2 emissions from geothermal power plant operations is to reinject coproduced CO_2 into the geothermal reservoir (Bonafin et al., 2019). CarbFix projects (Snæbjörnsdóttir et al., 2020) and Geothermal Emission Control (GECO) The H2020 project demonstrated the feasibility of capturing CO_2 from geothermal power plants, mixing it with the effluent geofluid, and then injecting it into the geothermal reservoir (Delerce et al., 2023; Leontidis et al., 2023). In Icelandic basalt, the injected geofluid-CO_2 mixture reacts with reservoir rocks, resulting in the mineral trapping of CO_2 such as calcite, ankerite, and dolomite at temperatures below 165 °C (Galeczka et al., 2022). On the contrary, the geofluid in the reservoir near the injection well has a pH of 6 to 8, where the injected CO_2 in the mixed geofluid is present mainly in bicarbonate form in Türkiye (Erol et al., 2022a; Erol et al., 2023a; Berndsen et al., 2024).

The typical temperatures for geothermal injection in binary power plants are approximately 70–80 °C, while in flash power plants, the usual temperature is 105 °C (DiPippo, 2016). The injection temperature must be adjusted to increase the mixing ratio of the dissolved amount of CO_2 in the effluent fluid. According to the saturation index analysis, at injection temperatures below 120 °C, the solubility of CO_2 increases. However, if the injection temperature is below 120 °C, a form of polymorph silica (quartz, amorphous silica, chalcedony, α- and β-cristobalite) and aluminosilicates, such as albite-low precipitation, may occur, affecting the amount of H_4SiO_4

* Correspondence: selcukerol@iyte.edu.tr

This work is licensed under a Creative Commons Attribution 4.0 International License.

in the fluid. According to Nicholson (1993), the solubility behavior of amorphous silica and quartz is important in geothermal studies, as they determine the supersaturation of silica and chalcedony, which is also crucial in some systems, such as Icelandic basalts, when fluid pathways change and expose volcanic glass. In cases presented in this study, the evolving thermodynamic conditions trigger the precipitating of different crystal structures of silica, such as chalcedony and cristobalite. Several conditions affect this supersaturation process: the initial degree of supersaturation, temperature, the salinity of the solution, pH of the solution, and the presence of particulate siliceous material. Among these parameters, pH value and temperature play a crucial role. Although all forms of silica have the same chemical formula, structural disparities and natural conditions distinguish the crystallization mechanisms of polymorphic silica to operate the growth of these different forms of silica. These mechanisms are discussed elsewhere, such as in Heaney (1993) and Richter-Feig et al. (2018). Studies by Gunnarsson and Arnorsson (2005) and Van den Heuvel et al. (2018) indicated that amorphous silica can typically deposit at surface pipelines and wellbores during the injection, causing operational problems in most geothermal systems. In this study, the various silica phases and carbonate reactions are inspected in the reservoir conditions when the injected CO_2-charged fluid is first in contact with the host rock minerals.

Current techniques of enhanced oil recovery (EOR), such as gas injection (CO_2), are frequently adequate and rarely impede the exploitation of hydrocarbon reservoirs that are situated within shallow carbonate- or quartz-rich lithologies (Blunt et al., 1993; Wang et al., 2013). However, CO_2 injection processes associated with geothermal reservoirs usually involve elevated temperatures and a variety of mineral reactions (Clark et al., 2020; Galeczka et al., 2022). It is essential to consider the role of CO_2-fluid–rock interaction and the kinetic rates of potential reactions under such conditions. Depending on the pressure, temperature, fluid composition, and minerals, mineral precipitation/dissolution impacts the pore space, and the permeability influences flow and, ultimately, the injection and production lifetime of a reservoir.

A variety of advances in computational access and speed have led to reactive transport models and stochastic simulations that more accurately predict processes in natural systems to address geochemical complexity (Aradóttir et al., 2012; Lüttge et al., 2013; Ancey et al., 2015). Furthermore, simulations are convenient for understanding phenomena that cannot efficiently be observed in the laboratory (Berndsen et al., 2024). However, validating and justifying the reactive transport modeling results is difficult due to the lack of measured data in a complex reservoir system. Stochastic modeling helps validate deterministic reactive transport results for estimating potential geochemical interaction outcomes by allowing for random variation in one or more inputs over time.

Reactive transport modeling has been used to obtain deterministic results of the chemical reactions of water-rock interaction. The rate laws and reaction-diffusion-advection process have been constructed traditionally from deterministic equations mostly in the form of nonlinear partial differential equations (PDE). However, the fluid flow in a porous medium has erratic spatial variability, and the chemical reactions may demonstrate a very complex behavior (Rubin, 1990). This spatial variation of flow and chaotic behavior of the chemical system can lead to stochastic reaction rates and reactivity.

Such complex chemical systems can be approximately described by stochastic differential equations (SDEs) such as the Fokker-Planck equation under some conditions (Risken, 1989). The SDEs are introduced with ordinary differential equations (ODEs), including stochastic noise terms derived from the underlying master equation (Erban and Chapman, 2020).

Another valuable approach to inspecting the chemical reactions based on stochastic simulation was developed by Gillespie (1976, 1977). The Gillespie stochastic simulation algorithm (SSA) is derived based on the propensity functions between chemical reactants and products used to calculate the time evolution of reactant concentrations. According to Stundzia and Lumsden (1996), the Gillespie SSA is particularly adapted to the computational investigation of such systems as it provides a precise solution to the related master equation for a chemical reaction in a well-mixed reaction volume. Furthermore, the Gillespie SSA tracks changes in the total numbers of each reactant species unit-by-unit. It is adapted to analyze systems with low reactant densities using continuum approximation-based techniques.

The parameters of a model are constant in most deterministic continuous models. The stochastic equivalent of this is to alter the constant in the random variables. The random variable has a constant value for each realization, but it may change depending on the probability distribution of the realization. Random variables, the most fundamental component of a stochastic model, consist of functions, rendering them objects with infinite dimensions.

This study analyzes the silica phase precipitation process with deterministic reactive transport modeling and stochastic reaction-diffusion-advection simulations. Ratouis et al. (2021) identified several feed zones along the injection wellbore, and the relevant flow routes between the injection and production wellbores were made utilizing a one-dimensional (1-D) reactive transport simulation to

assess the CO_2-geofluid-rock interaction at the geothermal site at the Hellisheidi basaltic geothermal reservoir. Similar to this assumption, we focused on a single feed zone of an injection wellbore in the Kızıldere geothermal reservoir in Türkiye to assess the precipitation of silica phases and carbonates in a reactive transport model. Moreover, a compartment-based stochastic simulation based on the Gillespie method is developed for the chemical reactions of silica phases and the carbonization process. This 1-D approach can provide a closer inspection near an injection wellbore, where we failed to capture the details in 3-D models in the previous studies (Erol et al., 2022a; Erol et al., 2023a).

2. Model setup

A 1-D reactive transport model and a compartment-based stochastic reaction-diffusion-advection domain are set up, representing a feed zone depth of the injection well (Figure 1). The advantage of this 1-D model is that it reduces the intensive computational effort, avoiding the additional complexity of the mineral rock interactions in the rest of the reservoir domain. The feed zones are determined based on the mud loss ratios from the well-log data (Huang et al., 2011).

The measured fluid chemistry data is recalculated with the PHREEQC software (Parkhurst and Appelo, 2013) at the corresponding pressure and temperature (PT) conditions of the reservoir and the injection line. The PHREEQC demonstrates possible secondary mineral phases in the considered system that are required to identify in the reactive transport simulation. The reactive transport model is constructed using the TOUGHREACT v1.2-Petrasim interface[1] (Xu et al., 2008) with the equations of state (EOS2) module, employing a two-phase water-CO_2 flow developed by Battistelli et al. (1997). The compartment-based Gillespie SSA is developed and implemented in MATLAB version 2022a (MATLAB, 2023[2]).

One critical parameter is to determine the thickness of each compartment and the spatial distance of the computational domain that affects the chemical equilibrium during the fluid flow. The equilibrium can be approximated when the Damköhler number, $Da = k.h/u$, is greater than 1 (Lichtner, 1996). Here u is the fluid velocity, k denotes the reaction rate, and h represents the thickness of each grid/compartment.

This suggests that $h > u/k$ is the contact length with the reactive surface. The time to reach a length of h can be regarded as the exposure time to achieve equilibrium in the aqueous concentrations. In contrast to those beyond h, all concentrations over spatial distances less than h will not have reached equilibrium (Binning and Celia, 2008).

Based on the information obtained from the field, the mass flow rate at the injection well is approximately 50 kg s^{-1}. The ionic strength of the effluent fluid is around 0.12 molality at 100 °C. The partial pressure of CO_2 is lower than 1 MPa near the injection well since this well is operated for injection of the effluent fluid without CO_2 over a couple of years. The solubility of CO_2 in the effluent fluid should be kept smaller than 0.1 mol kg^{-1} to maintain the injection as a single-phase flow.

Assuming that the mass flow rate in a feed zone is a maximum of 5 kg s^{-1}. This value is approximated based on the total mass flow rate of the well and the mud-loss data obtained from the well logs (Erol et al., 2023b). The flow velocity, u, can be around 2×10^{-4} m s^{-1} in a 5×5 m^2 cross-section area. Considering one of the slowest reaction rates , such as quartz dissolution at 0.0014 s^{-1} at 120 °C (Rimstidt and Barnes, 1980), the value of h should be greater than 0.1429, so h is fixed to 0.2 m. The grids are constructed using the regular gridding method. The total number of grids is 250 along a 50 m model length for stochastic and reactive transport simulations.

The initial CO_2 mass fraction at reservoir conditions is around 3.7% (Haizlip et al., 2016), whereas the mass fraction of the mixed CO_2 is about 0.28% of the injection rate of the effluent fluid (e.g., 180 tones per hour). This means that around 4.7 kt/yr of CO_2 will be injected if the injection is persistent as a single-phase flow.

The chemistry of the geofluid and the flow conditions are applied at the leftmost grid (Figure 1). The injection mass flow rate of the effluent fluid is fixed to 5 kg $s^{-1,}$ and 0.014 kg s^{-1} of CO_2 is applied to mix into the fluid. The gaseous phase is not observed.

Based on a real injection history of an injection well in the field of Kızıldere, the simulation is run for 10 years in total. For the first 3 years, the well was idle. During this period, the estimated mass fraction of CO_2 around the injection well at 2300 m depth was around 3% (Erol et al., 2022a). Therefore, the model is run for its natural state over 3 years, and the chemical system nearly reaches quasisteady state conditions. In the following 2 years, only the effluent fluid is injected, and then CO_2-fluid mixture injection commences and continues for 5 more years. The geochemical interaction is evaluated at temperatures 80 °C, 90 °C, 105 °C, 110 °C, and 120 °C both to inspect fluctuating injection fluid temperature due to the mixing process and to represent the typical injection temperatures

[1]Rockware (2023). Graphical interface for the TOUGHREACT v1.2 simulator Webpage https://www.rockware.com/product/petrasim/ [accessed 06 June 2023].

[2]MATLAB (2023). Multi-paradigm numerical computing software and fourth-generation programming language. Website https://www.mathworks.com [accessed 04 September 2023].

in binary and flash geothermal power plants. The results are compared particularly for possible calcite, albite, and silica phases along the feed zone. For detailed analysis, calcite was selected due to its relatively fast reaction kinetic rates compared to other carbonate minerals and its tendency to react with the injected CO_2. Silica phases and albite were chosen for critical solubility limits below 120 °C temperature. The initial reservoir temperature at the slotted liner depth is around 220 °C. The corresponding depth is 2300 m.

The mineral compositions are inspected to represent metasediment layers, such as muscovite and quartz schist, which are typically found in geothermal reservoir rocks located in the Büyük Menderes Graben, in western Türkiye (Alçiçek et al., 2007). The top of the metasediment reservoir is around 1000 m, reaching 3850 m at the bottom.

Based on the tracer test analysis, the feed zone's initial equivalent permeability and porosity values are set to 1×10^{-13} m^2 and 0.03, respectively (Erol et al., 2022b).

2.1. Reactive transport

The physical processes that contribute to the transport of the inert solutes are advection, molecular diffusion, and reaction. The governing deterministic PDE describes the reactive transport process in 1-D cartesian coordinates in porous media:

$$\frac{\partial \phi C_i}{\partial t} = \phi D_s \frac{\partial^2 C_i}{\partial x^2} - \phi u_i \frac{\partial C_i}{\partial x} - \sum_{r=1}^{N_a} \upsilon_a R_a - \sum_{r=1}^{N_m} \upsilon_m R_m \quad (1)$$

where t is time, C is the i^{th} solute concentration, and R_a and R_m are the reaction rates of aqueous species and minerals, respectively. D_s is the dispersion coefficient of the solutes, u_i, *is* the flow velocity along the x-direction, N is the number of reactions, υ is the stochiometric coefficient, and ϕ is the porosity of the porous or fractured medium.

Corresponding equilibrium constant K for the considered reactions with α-quartz, chalcedony, α-cristobalite, amorphous silica, albite-low, and calcite were expressed as:

$$\log(K) = a\ln(T) + b + cT + dT^{-1} + eT^{-2} \quad (2)$$

where the T is the temperature in Kelvin, and the interpolation coefficients can be found in Table 1.

For both TOUGHREACT and PHREEQC programs, the Thermoddem thermodynamic database developed by Blanc et al. (2012) has been implemented. The fluid chemistry data is given in Table 2, used in the TOUGHREACT. The ionic strength of the fluid is around 0.12 molality.

The mineral compositions given in Table 3 are constituted based on the experimental evaluations of Berndsen et al. (2024), which are representative of the geothermal reservoir. Five injection variants are considered for each rock type with identical fluid compositions to make a comparative assessment.

The kinetic rate coefficients and activation energy of minerals are specified based on the parameters given by Palandri and Kharaka (2004) and provided in Table 4. The grain size of minerals is assigned between 8.5×10^{-4} and 1×10^{-4} m, and the specific surface area of minerals is between 1.1 and 2 cm^2 g^{-1}.

2.2. Gillespie stochastic simulation algorithm

For the stochastic simulation of chemical reaction systems, the Gillespie SSA presents an accurate technique used to calculate the reactant concentration over time. The Gillespie algorithm uses the number of possible events and the rate at which events occur to generate the time until the next event randomly. The Gillespie method is implemented into a compartment-based model to simulate chemical reactions along the feed zone (Figure 1).

Compartmental models are constructed by combining sections of linked stirred tanks or mixing chambers first proposed by Thakur et al. (1972) to model primarily biological systems. The components of the system are assumed to be uniformly and homogeneously concentrated and promptly combined. Chemical species concentrations or molar quantities are the state variables. First-order rate equations are typically used to model chemical reactions (Matis and Wehrly, 1979; Bassingthwaighte et al., 2012). The interaction between compartments is assumed as the reflective boundary condition as back-and-forth jumps, including drift velocity, and the jumping rate between compartments is identical to all compartments. The compartment-based Gillespie SSA in this study is derived according to the methodology of Erban and Chapman (2020).

Table 1. Interpolation coefficients of minerals used in the empirical Eq. 2.

Mineral	a	b	c	d	e
α-Quartz	53.936	−353.75	-4.188×10^{-2}	2.1804×10^{4}	-1.5943×10^{6}
Chalcedony	53.554	−351.23	-4.1615×10^{-2}	2.173×10^{4}	-1.5846×10^{6}
α-Cristobalite	53.971	−354.40	-4.1703×10^{-2}	2.2114×10^{4}	-1.6002×10^{6}
Amorphous silica	53.611	−353.40	-4.0434×10^{-2}	2.2631×10^{4}	-1.6540×10^{6}
Albite-low	254.77	-1.6580×10^{3}	-2.1973×10^{-1}	1.0358×10^{5}	-6.4383×10^{6}
Calcite	134.48	-8.5010×10^{2}	-1.3947×10^{-1}	4.6881×10^{4}	-2.6591×10^{6}

Table 2. Calculated fluid chemistry for deep reservoir and injection-line conditions. [a] Measured temperature. [b] Calculated fluid pH at the corresponding temperature with the PHREEQC program. Reservoir fluid chemistry is equilibrated with approximately 3% of CO_2 weight fraction.

Parameter	Reservoir		Injected fluid without CO_2 mixing				
	Mica schist	Quartz schist					
T-pH (°C)	220 [a]	220 [a]	80	90	105	110	120
pH	8.12 [b]	8.06 [b]	9.1 [b]	8.97 [b]	8.86 [b]	8.83 [b]	8.76 [b]
Primary species	Amount (mol kg^{-1})						
Al^{+3} ($\times10^{-24}$)	0.011	1.8	52	19.3	5.2	3.4	1.46
Br^- ($\times10^{-5}$)	1.52	1.52	1.65	1.65	1.65	1.648	1.647
Ca^{+2} ($\times10^{-5}$)	0.061	0.0025	5.11	5.05	4.77	4.67	4.45
Cl^- ($\times10^{-3}$)	3.97	3.77	4.68	4.68	4.68	4.68	4.68
F^- ($\times10^{-3}$)	1.2	1.2	1.5	1.5	1.5	1.496	1.496
Fe^{+2} ($\times10^{-8}$)	0.47	0.093	3.56	3.35	2.46	2.1	1.41
H^+ ($\times10^{-8}$)	1.08	1.24	0.105	0.127	0.164	0.177	0.204
HCO_3^- ($\times10^{-3}$)	610	610	2.68	2.75	2.86	2.89	2.96
K^+ ($\times10^{-3}$)	4.66	4.72	6.07	6.07	6.07	6.07	6.07
Mg^{+2} ($\times10^{-7}$)	0.248	0.132	5.28	5.1	4.71	4.55	4.18
Mn^{+2} ($\times10^{-7}$)	0.0175	0.0218	4.22	3.51	2.49	2.18	1.63
Na^+	0.0318	0.0325	0.0678	0.0678	0.0678	0.0678	0.0678
H_4SiO_4 ($\times10^{-3}$)	4.62	6.32	4.65	4.68	4.73	4.75	4.81

Basically, the rate of jumping of chemical species between compartments can be depicted as:

$$(\text{reactant/product})_1 \underset{k_2^-}{\overset{k_1^+}{\rightleftarrows}} (\text{reactant/product})_2 \underset{k_3^-}{\overset{k_2^+}{\rightleftarrows}} \cdots \underset{k_K^-}{\overset{k_{K-1}^+}{\rightleftarrows}} (\text{reactant/product})_K \quad (3)$$

where K represents the number of compartments. As the reaction takes place, in each compartment, the concentration of a reactant or product is changed with the advection-diffusion process controlled by the, k_i^+, k_i^- jump rates from the i^{th} compartment. These rates must be positive and can be given as follows:

$$k_i^+ = \frac{D_s}{h^2} + \frac{f(x_i)}{2h}, \quad k_i^- = \frac{D_s}{h^2} - \frac{f(x_i)}{2h} \quad (4)$$

where x_i is the center of the i^{th} compartment ($x_i = i.h - h/2$), $f(x)$ is the drift velocity that can be assigned as the flow velocity in the porous medium, h is the compartment thickness (0.2 m), and D_s is the dispersion coefficient of the solutes that can be estimated as:

$$D_s = D_0 + u\lambda_L \quad (5)$$

Table 3. Mineral contents of the rock types.

Rock type	Primary minerals (volume fractions)	Secondary minerals
Muscovite-schist	α-quartz 58%, muscovite (ord) 25%, montmorillonite-Na 13%, hematite 2%, andalusite 1%, paragonite 1%	Albite-low, amorphous silica, calcite, chalcedony, α-cristobalite, chlorite, dolomite (ord), pyrite, siderite, talc
Quartz-schist	α-quartz 91%, muscovite (ord) 3%, hematite 2%, andalusite 3%, epidote 1%	Albite-low, amorphous silica, calcite, chalcedony, α-cristobalite, dolomite (ord), paragonite, pyrite, montmorillonite-Na, siderite, talc

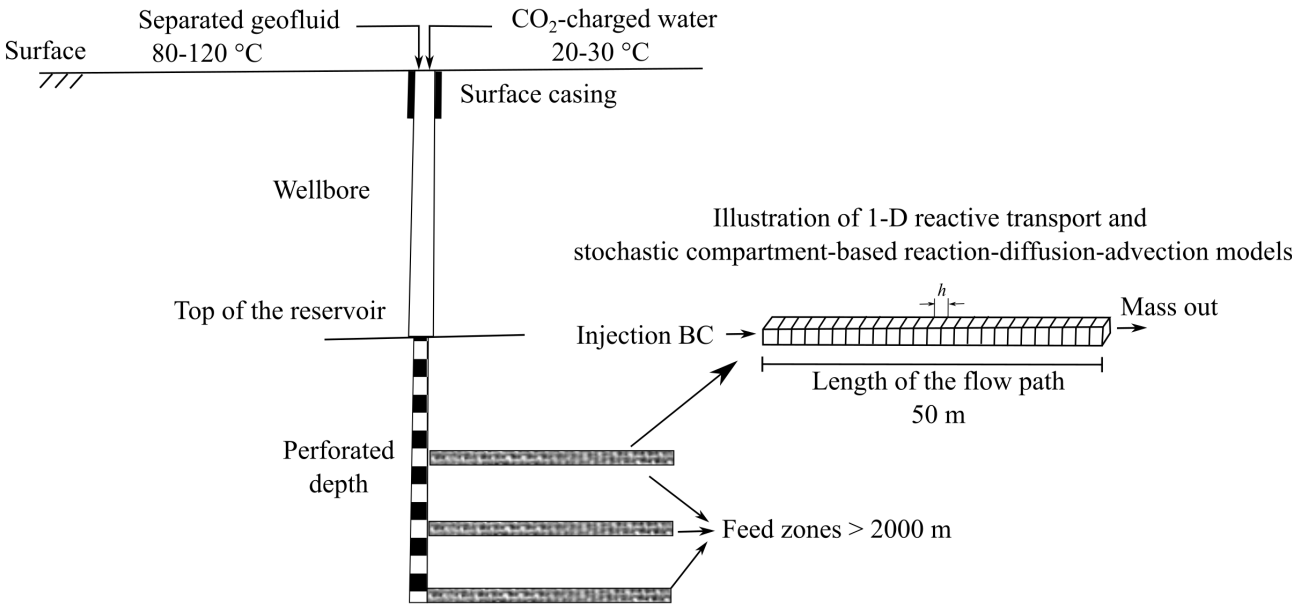


Figure 1. Illustration of an injection wellbore and feed zones delineated as reactive transport and stochastic compartment-based model.

where D_0 is the molecular diffusivity coefficient of the solutes, u is the flow velocity, and λ_L is the longitudinal dispersion that can be typically set around 1 m for a length of 50 m models (Molina-Giraldo et al., 2011). In that case, D_s is roughly 2×10^{-4} m^2 s^{-1} in our simulations based on the flow velocity $u = 2 \times 10^{-4}$ m s^{-1}.

In a system comprising j chemical reactions, where $\alpha_i(t)$ represents the propensity function of the i^{th} reaction, $i = 1, 2, \ldots, j$, at time t, that is, $\alpha_i(t).dt$ denotes the probability of the i^{th} reaction occurring within the time interval $[t, t + dt)$.

The considered chemical reactions for the stochastic computation are given as follows:

$$SiO_2(\alpha\text{-Quartz}) + 2H_2O \xrightarrow{R_1} H_4SiO_4 \quad (6)$$

$$H_4SiO_4 \xrightarrow{R_2} 2H_2O + SiO_2(\text{Chalcedony}) \quad (7)$$

$$H_4SiO_4 \xrightarrow{R_3} 2H_2O + SiO_2(\alpha\text{-Cristobalite}) \quad (8)$$

$$H_4SiO_4 \xrightarrow{R_4} 2H_2O + SiO_2(\text{Amorphous silica})$$

$$3H_4SiO_4 + Al^{3+} + Na^+ \xrightarrow{R_5} 4H + 4H_2O + NaAlSiO_8(\text{Albite-low}) \quad (10)$$

$$Ca^{2+} + CO_3^{2-} \xrightarrow{R_6} CaCO_3(\text{Calcite}). \quad (11)$$

Here R represents the reaction rates as mol kg^{-1} s^{-1}. The calculated range of reaction rates is taken from the TOUGHREACT simulation for the Gillespie SSA computations.

The propensity functions for basic chemical reactions given above are estimated as follows:

$$\alpha_1 = \alpha\text{-Qz}((1{:}n\text{-}1),\, t).H_2O((1{:}n\text{-}1),\, t)(H_2O((1{:}n\text{-}1),\, t) - 1).\, k_1^+ / v^2 + \alpha\text{-Qz}((2{:}n),\, t).H_2O(2{:}n,\, t)(H_2O(2{:}n,\, t) - 1).\, k_1^- / v^2$$

$$\alpha_2 = k_2^+ H_4SiO_4((1{:}n\text{-}1),\, t) + k_2^- H_4SiO_4((2{:}n),\, t) \quad (13)$$

$$\alpha_3 = k_3^+ H_4SiO_4((1{:}n\text{-}1),\, t) + k_3^- H_4SiO_4((2{:}n),\, t) \quad (14)$$

$$\alpha_4 = k_4^+ H_4SiO_4((1{:}n\text{-}1),\, t) + k_4^- H_4SiO_4((2{:}n),\, t) \quad (15)$$

$$\alpha_5 = 3H_4SiO_4((1{:}n\text{-}1),\, t).(H_4SiO_4((1{:}n\text{-}1),\, t) - 1).(H_4SiO_4((1{:}n\text{-}1), t) - 2).k_5^+ / v^2\, Al^{3+}((1{:}n\text{-}1), t).Na^+((1{:}n\text{-}1),\, t) + 3H_4SiO_4((2{:}n),\, t).(H_4SiO_4((2{:}n),\, t) - 1).(H_4SiO_4((2{:}n),\, t) - 2).k_5^- / v^2\, Al^{3+}((2{:}n),\, t).Na^+((2{:}n),\, t) \quad (16)$$

$$\alpha_6 = Ca^{2+}((1{:}n\text{-}1),\, t).CO_3^{2-}((1{:}n\text{-}1),\, t).\, k_6^+ / v + Ca^{2+}((2{:}n),\, t).CO_3^{2-}((2{:}n),\, t).\, k_5^- / v \quad (17)$$

$$\alpha_0 = \alpha_1 + \alpha_2 + \alpha_3 + \alpha_4 + \alpha_5 + \alpha_6, \quad (18)$$

where n is the number of compartments, and the reactants and solutes are represented by their mol and mol kg^{-1} amounts, respectively.

Then, the following four steps comprise the Gillespie SSA to control the number of events at time t (Gillespie, 2001):

- Create two random numbers, r_1 and r_2, uniformly distributed between 0 and 1. A random number generator is utilized in MATLAB.
- Calculate the propensity function $\alpha_i(t)$ of each reaction as follows:

$$\alpha_0 = \sum_{i=1}^{N} \alpha_i(t)$$

- Calculate the time when the subsequent chemical reaction takes place as $t + \tau$, where

$$\tau = \frac{1}{\alpha_0} \ln\left(\frac{1}{r_1}\right),$$

- Calculate which reaction occurs at time $t + \tau$. Find j such that

$$\text{If } r_2 < \frac{1}{\alpha_0} \sum_{i=1}^{j} \alpha_i(t)$$

If the following reaction is the jump to the right (e.g., $\alpha\text{-}Qz_j(t) \rightarrow \alpha\text{-}Qz_{j+1}(t)$), the amount of moles of the species in the compartments changes as follows:

$$\begin{cases} \text{Reactant}_j(t+\tau) = \text{Reactant}_j(t) - R_j t \\ \text{Reactant}_{j+1}(t+\tau) = \text{Reactant}_{j+1}(t) + \text{R}_\text{j}\text{t} \\ \text{Reactant}_i(t+\tau) = \text{Reactant}_i(\text{t}) \text{ for } i \neq j, i \neq j+1 \end{cases}$$

$$\begin{cases} \text{Product}_j(t+\tau) = \text{Product}_j(t) + R_j t \\ \text{Product}_{j+1}(t+\tau) = \text{Product}_{j+1}(t) - R_j t \\ \text{Product}_i(t+\tau) = \text{Product}_i(t) \text{ for } i \neq j, i \neq j+1 \end{cases}$$

And if the subsequent reaction is the jump to the left (e.g., $\alpha\text{-}Qz_j(t) \rightarrow \alpha\text{-}Qz_{j-1}(t)$), then the amount of moles of the species in the compartments change as follows:

$$\text{If } r_2 \geq \frac{1}{\alpha_0} \sum_{i=1}^{j-1} \alpha_i(t)$$

$$\begin{cases} \text{Reactant}_j(t+\tau) = \text{Reactant}_j(t) - R_j t \\ \text{Reactant}_{j-1}(t+\tau) = \text{Reactant}_{j-1}(\text{t}) + R_j t \\ \text{Reactant}_i(t+\tau) = \text{Reactant}_i(t) \text{ for } i \neq j, i \neq j+1 \end{cases}$$

$$\begin{cases} \text{Product}_j(t+\tau) = \text{Product}_j(t) + R_j t \\ \text{Product}_{j-1}(t+\tau) = \text{Product}_{j-1}(t) - R_j t \\ \text{Product}_i(t+\tau) = \text{Product}_i(t) \text{ for } i \neq j, i \neq j+1 \end{cases}$$

- if $r_2 \geq \sum_{i=1}^{K-1} \alpha_1/\alpha_0$, then find $j \in \{2, 3, 4 \ldots, K\}$

$$r_2 \geq \frac{1}{\alpha_0} \left(\sum_{i=1}^{K-1} \alpha_i(t) + \sum_{i=2}^{j-1} \alpha_i(t) \right)$$

and

$$r_2 < \frac{1}{\alpha_0} \left(\sum_{i=1}^{K-1} \alpha_i(t) + \sum_{i=2}^{j} \alpha_i(t) \right)$$

Then the j^{th} reaction takes place, so update the numbers of reactants and products of the j^{th} reaction and continue with the first step for time $t + \tau$.

3. Results

Figure 2 depicts the variations in the solubility of silica phases in the geofluid concerning temperature. The metastable limits of silica polymorphs solubilities (e.g., α-Qz, Chd, Crs, and Aph-Si) and Ab-low are plotted based on the Thermoddem thermodynamic database (Blanc et al., 2012). The results of the reactive transport simulations are demonstrated as muscovite schist (o marker) and quartz schist (**x** marker). These results represent temporal and spatial variability with the error bars through the deterministic reactive transport simulation TOUGHREACT.

The amount of H_4SiO_4 in the solution changes depending on the constituent of the two types of schist and the injection temperature. Particularly, the amount of quartz in the rock affects the concentration of the H_4SiO_4 in the solution, so the muscovite schist case has more H_4SiO_4 in the solution. Typically, the constituent atoms are arranged in a regular way, such as crystalline silica-based quartz in a crystalline solid. However, at elevated temperatures, the system enters the metastable supersaturated state. In Figure 2, it can be seen for the quartz schist scenario that the metastable limit of chalcedony and partially of α-cristobalite is reached and goes above as cooling continues. In that case, crystal nucleation and growth of chalcedony and α-cristobalite may occur, and the silica atoms may have no long-range order. On the other hand, in the muscovite schist scenario, the supersaturation tends to move beyond the solubility limits of α-cristobalite and amorphous-silica due to the high H_4SiO_4 concentration in the solution.

Concerning binary (80 °C) and flash power plant (105 °C) injection temperatures, the amount of H_4SiO_4 in the fluid is below the metastable limit of Aph-Si, but other forms of silica precipitation can be seen in both muscovite and quartz schist systems. However, Aph-Si may precipitate in the muscovite schist layer in binary injection temperature.

Figure 3 shows the comparison results of the geochemical interaction process in the TOUGHREACT model along the distance at the last simulation year (10th year) when the system reaches a quasisteady state with the

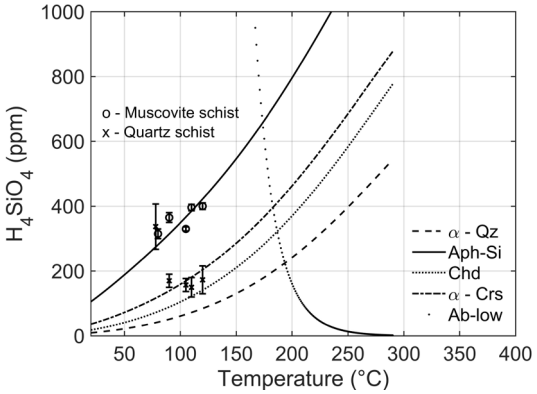


Figure 2. Variation in the solubility of silica phases and albite-low over temperature. The lines represent the excess of the metastable solubility limit of silica phases and the albite-low. The markers and error bars depict temporal and spatial variability of the fluid solutions at the injection temperatures between 80 °C and 120 °C in the model. Abbreviations of minerals are given in Table 4.

Table 4. Kinetic parameters used in reactive transport simulations. [a] Abbreviation is used for names of minerals (Whitney and Evans, 2010). [b] Palandri and Kharaka (2004), [c] Based on the sieve analysis.

Minerals	Abb. [a]	Kinetic rate constant k_{25} (mol m^2 s^{-1}) [b]	The activation energy (kJ mol^{-1}) [b]	Grain size (m) [c]	Average specific surface area (cm^2 g^{-1}) [c]
Albite-low	Ab-low	2.75×10^{-13}	65	1×10^{-4}	2
Andalusite	And	3×10^{-8}	38	2.5×10^{-4}	2
Calcite	Cal	1×10^{-6}	25	8×10^{-5}	2
Chalcedony	Chd	4×10^{-13}	74	8.5×10^{-4}	2
Cristobalite (alpha)	α-Crs	5×10^{-13}	65	8.5×10^{-4}	2
Chlorite	Chl	6.4×10^{-17}	16	5×10^{-4}	2
Dolomite (ord)	Dol	2.5×10^{-9}	50	1×10^{-4}	2
Epidote	Ep	1×10^{-12}	70	8.5×10^{-4}	2
Hematite	Hem	2.51×10^{-15}	66	2.5×10^{-4}	1.1
Paragonite	Pg	1×10^{-13}	22	5×10^{-4}	2
Pyrite	Py	2.8×10^{-5}	57	2.5×10^{-4}	1.1
Montmo.-Na	Mnt-Na	1.65×10^{-14}	35	1.5×10^{-5}	11
Muscovite (ord)	Ms	1.4×10^{-13}	22	4.2×10^{-4}	2
Quartz (alpha)	α-Qz	2×10^{-14}	90	8.5×10^{-4}	2
Siderite	Sd	1×10^{-8}	50	2.5×10^{-4}	2
Talc	Tlc	1×10^{-12}	42	2.5×10^{-4}	2

CO_2-fluid injection. Two different rock types are inspected at five different injection temperatures over time.

As the injection commences, the temperature of the model domain quickly drops in a couple of months from the initial reservoir temperature to the applied boundary injection temperature along the distance. At the beginning of the effluent fluid injection, the injectate mixes with the native reservoir fluid which has 3% CO_2, increasing the pH from 6.5 to above 8, which also affects the supersaturation process. It is seen that the amount of H_4SiO_4 in the solution varies depending on the rock type. In the muscovite schist scenario, the amount of H_4SiO_4 in the solution is relatively more significant than in the quartz schist scenario, likely due to the less surface area of quartz in the muscovite schist limiting the reactions with H_2O to produce H_4SiO_4 (Figures 3a and 3b). Temperature is also a critical factor

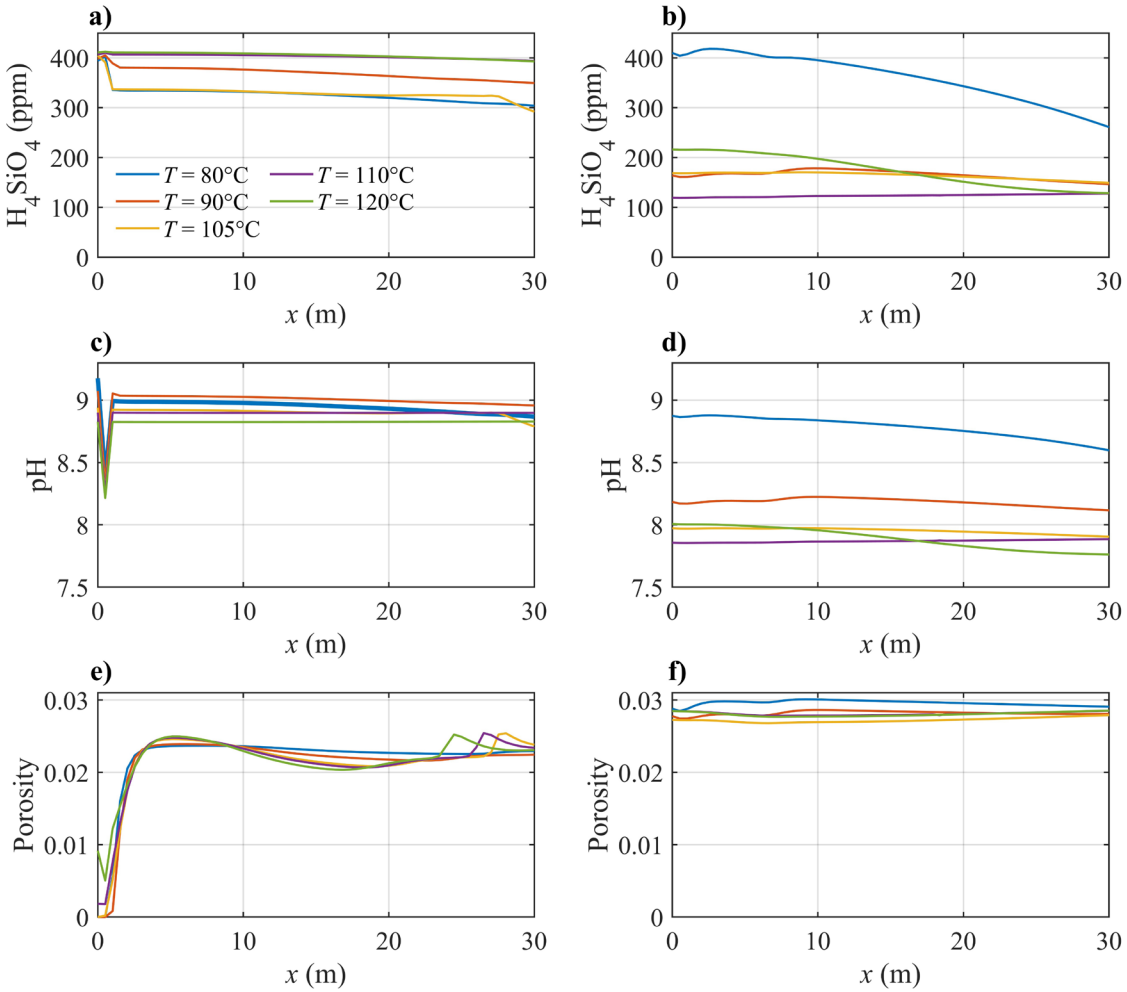


Figure 3. The injection takes place at $x = 0$. Muscovite schist (a, c, and e); Quartz schist (b, d, and f) scenario result over time at a depth of 2300 m along the feed zone distance.

in this reaction. Furthermore, the amount of H_4SiO_4 does not show a proportional change concerning the injection temperature. For instance, the H_4SiO_4 concentration in the muscovite schist at 90 °C is more significant than at 105 °C, whereas the reverse situation could be expected compared to other temperature cases. This can be attributed to the H_4SiO_4 consumption that may have occurred due to different silica types exceeding the metastable limit at some temperature conditions (Figure 2). The metastable limit estimations were obtained using the identical thermodynamic database (Thermoddem database).

As the pH slightly decreases in the solution at the injection boundary on the left-hand side (Figure 3c), it affects the supersaturation process of most of the minerals, which, in turn, changes porosity (Figure 3e). Gunnarsson and Arnorsson (2005) state that a slight variation in the pH value by 0.2–0.4 can significantly impact the degree of saturation for minerals with pH-dependent solubilities such as hydroxides, calcite, and magnesium. Moreover, the H_4SiO_4 in the solution can also be consumed by other Mg- or Al-bearing silicates. In the muscovite-schist scenario, calcite (approximately 3% vf) and hematite (approximately 1% vf) precipitations are observed as secondary mineral phases at the two grids where the CO_2-fluid mixture enters the domain that affects the pore space plugged completely (Figures 3e and 4a). Concerning fracture systems, the precipitation of secondary minerals can also plug the fractures. According to Griffiths et al. (2016), fracture plugging occurred in a sandstone geothermal reservoir, and fractures were filled with carbonates and secondary silica minerals.

Calcite precipitation is also observed in the quartz schist case at different temperatures (Calcite approximately 1×10^{-4}% vf), but the amount is insufficient to plug the pores (Figures 3f and 4b). These results indicate that the injected CO_2 may quickly react at the reservoir entrance and can

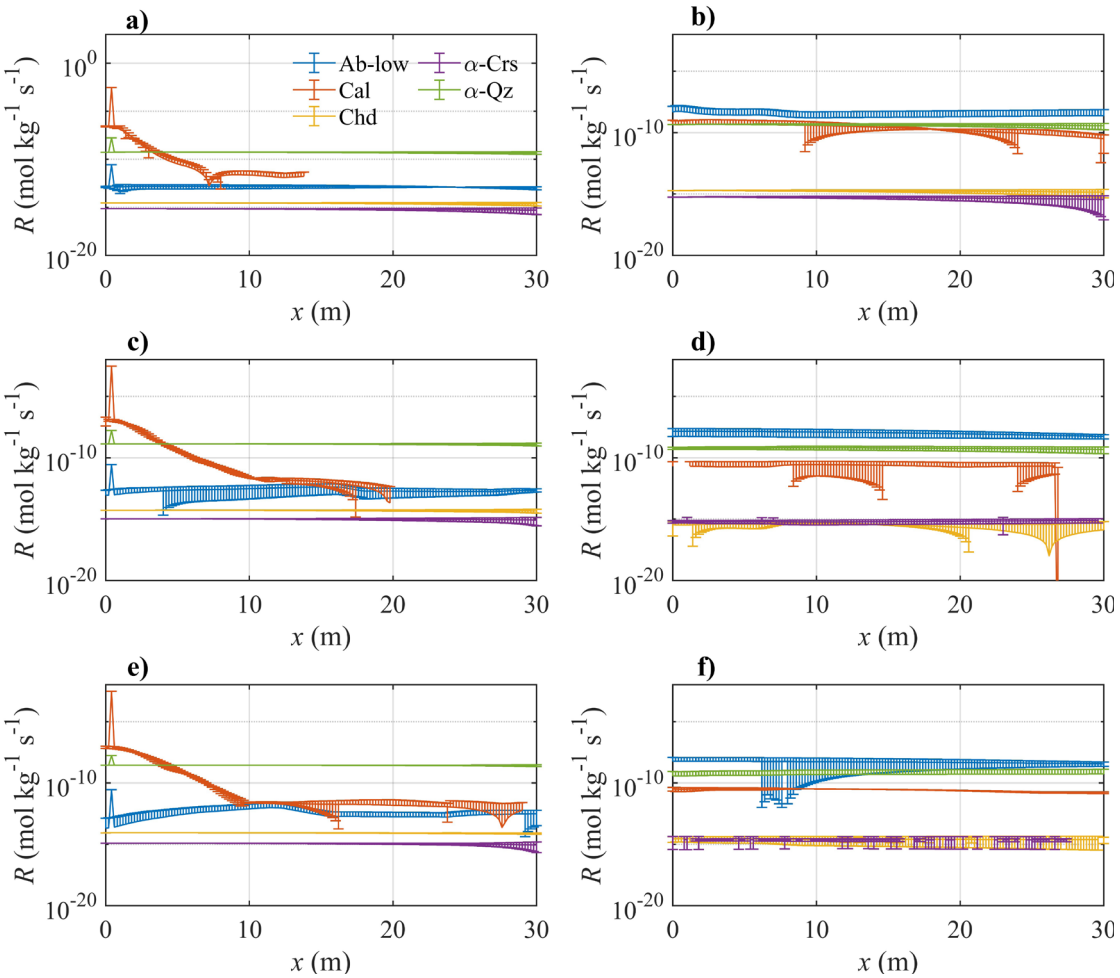


Figure 4. Reaction rates of secondary minerals and α-quartz at a depth of 2300 m along the feed zone length. The injection takes place at $x = 0$. Muscovite schist (a, c, and e); Quartz schist (b, d, and f) scenario results. a) and b) at 80 °C; c) and d) at 105 °C; e) and f) at 120 °C. Abbreviations of minerals are given in Table 4.

Table 5. Maximum reaction rates of chemical reactions obtained from Figure 4. The reaction rates are multiplied by a random number between 0 and 1 in each realization in Gillespie SSA.

Chemical reaction equation	Maximum reaction rates R (mol kg^{-1} s^{-1})	
	Muscovite schist	Quartz schist
α-Quartz (Eq.6)	5.4×10^{-10}	6.5×10^{-10}
Chalcedony (Eq. 7)	3×10^{-17}	6×10^{-16}
α-Cristobalite (Eq. 8)	3×10^{-17}	6×10^{-16}
Albite-low (Eq. 10)	4.5×10^{-13}	1.4×10^{-8}
Calcite (Eq. 11)	2×10^{-8}	3.7×10^{-11}

affect the permeability due to the calcite precipitation in the muscovite schist layers. In contrast, CO_2 interaction with minerals is less in the quartz schist layers.

The calcite precipitation outcome shows some variation compared to the results reported in a prior study on 3-D reactive transport modeling by Erol et al. (2023a). Several reasons for these variations can be identified: i) the computational accuracy regarding the chemical equilibrium is not achieved in the 3-D model. The grid size in the vicinity of the wellbore was 255 m^2 in the 3-D model, whereas it is 25 m^2 in the current 1-D model; ii) the mass and heat fluxes in three dimensions affected the chemical equilibrium in the grid in which we have anisotropic permeability component.

Several techniques can be applied to create a 3-D reactive transport model with an identical level of detail as a 1-D model. The computational effort associated with the intricate coupling between the flow, heat, solute transport, and reactive chemical processes is one of the significant challenges in reactive transport modeling. The large spatial and temporal variabilities make studying reactive processes at a large reservoir scale difficult. Heat and mass fluxes originating outside of the examined model domain can be computed in a large-scale model, ignoring the geochemical interactions, and applied at the border cells of a localized model, including reactive transport to lessen the computing burden. Thus, the number of grids can be reduced, but the size of the grids can be downsized to capture local chemical equilibrium near the injection wellbore.

Figure 4 demonstrates the reaction rates of chalcedony, α-cristobalite, albite-low, and calcite, precipitated as secondary minerals, and α-quartz as the primary dominant mineral along the distance in both rock types. Only in the quartz schist scenario, a small amount of amorphous silica is precipitated at 80 °C. Therefore, we ignored it in Figure 4. The reaction rates of those minerals are depicted at the injection temperatures of 80 °C (Figures 4a and 4b), 105 °C (Figures 4c and 4d), and 120 °C (Figures 4e and 4e).

The reaction rates of all these minerals slightly vary as temperature changes in each rock type (Figures 4a, 4c, 4e and 4b, 4d, 4f). Error bars remark the temporal variation of reaction rates of secondary minerals along the distance. Maximum values are always obtained as the chemical equilibrium in each grid is achieved after a couple of months of continuous injection. Calcite propagates further away from the leftmost grid to the end of the column as the injection temperature rises. Moreover, calcite precipitation indicates that the CO_2 reacts and is trapped in the mineral form as soon as it enters a muscovite schist layer (Figure 4a). The reaction rate of α-quartz remains uniformly constant across distances in both rock types, resulting in the formation of H4SiO4 as a product. This process leads to the precipitation of chalcedony and α-cristobalite, characterized by the slowest reaction rates. Albite-low has the highest reaction rate in quartz schist compared to the muscovite schist scenario (Figures 4a and 4b). The flow velocities may affect the distribution of kinetic rates, pH, and amounts of albite-low precipitated. In muscovite schist, the porosity approaches zero at the first 5 m distance, affecting the permeability. Therefore, the kinetic rates and pH may be affected. The precipitated amount of secondary minerals varies along the length at some temperatures, and reaction rates may differ at each grid.

Validation of the precipitation process of these minerals and their randomness to react along the distance is essential to evaluate and validate the deterministic reactive transport simulations. The Gillespie SSA results are compared with the TOUGHREACT simulations in Figure 5 for muscovite schist and Figure 6 for quartz schist scenarios. In the Gillespie SSA, the kinetic rates of minerals are randomly selected within a specified range at each compartment, as outlined in Table 5. Specifically, the maximum kinetic rate is multiplied by a random number ranging from 0 to 1. Consequently, the reaction rate varies, typically falling at least one to five orders of magnitude lower than the maximum value in each realization.

Figure 5 demonstrates validation of the TOUGHREACT results with Gillespie SSA modeling. Except for α-quartz, the initial amount of all other secondary minerals is zero. The initial amounts of aqueous species specified in Gillespie SSA can be found in Table 2 (i.e., H_4SiO_4, Na, Ca^{+2}, and Al^{+3}).

The stochastic results slightly differ from those of the deterministic TOUGHREACT. Several reasons can be accounted for: i) most of the minor chemical reactions in the system consuming H_4SiO_4, such as epidote, are ignored and not assigned as an input in the system to avoid more extensive computations. ii) the random reaction rate specified in each compartment leads to minor discrepancies. Stochastic simulation still predicts a similar trend of mineral dissolution or precipitation compared to the TOUGHREACT simulations along the feed zone. Moreover, the Gillespie SSA approach shows that mineral reactions can be assessed and help optimize the injection process in a complex geothermal reservoir. The degradation of quartz and H_4SiO_4 increments are consistent in the system as described in Eq. 9 (Figures 5a and 5b). The produced H_4SiO_4 is quickly consumed by other reactions to form chalcedony, α-cristobalite, and albite-low as secondary minerals at the beginning of the feed zone where the injection fluid-CO_2 enters the muscovite schist layer. Figure 5f shows that CO_2 reacts rapidly with carbonate to form calcite due to pH levels (Figure 3c). The calcite precipitation dominantly occurs at the first 10 m, when it plugs the pores, and porosity decreases to zero (Figure 3e). As we expressed the reasons above, this outcome of the 1-D model is different from the 3-D reactive transport modeling study presented in Erol et al. (2023a). Although the 1-D model is limited to representing surrounding heat fluxes affecting the chemical equilibrium, the resolution of the 1-D model captures the calcite precipitation occurring in local zones near the wellbore due to the smaller grid size. Therefore, the dissipation of CO_2 from the wellbore through the feed zone may have been hindered in some locations in the muscovite schist layer.

Figure 6 demonstrates the results of the quartz schist scenario. Gillespie SSA estimations roughly fit the deterministic reactive transport results. The Gillespie SSA results show different trends for α-quartz and H_4SiO_4 at the

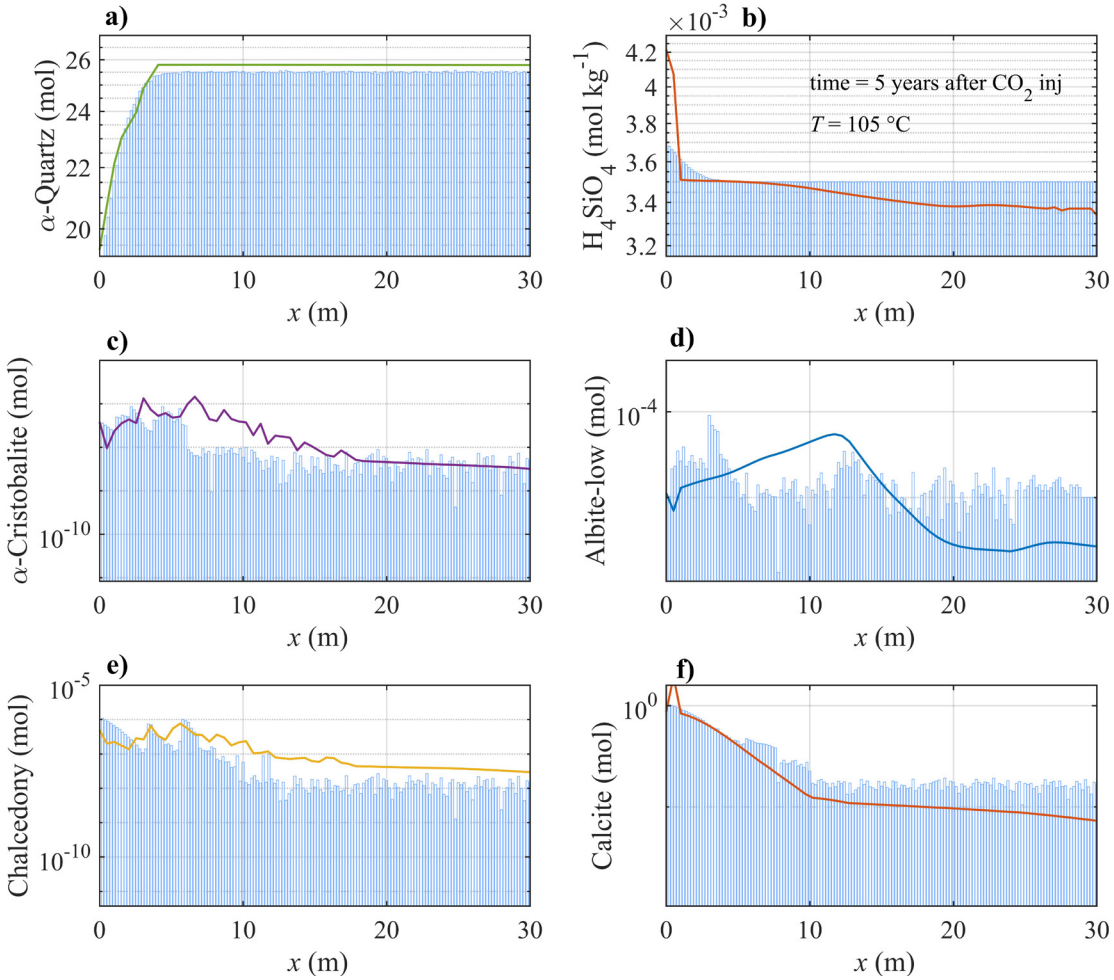


Figure 5. Comparison of the muscovite schist scenario's stochastic and deterministic reactive transport results over feed zone distance. Temperature is 105 °C in all subplots. Injection takes place on the leftmost grid. Blue bars represent stochastic computation; lines denote the TOUGHREACT simulation results.

leftmost grids where the injected fluid enters the domain. The mismatch between the deterministic and stochastic approaches can be again attributed to the previously explained reasons above for Figure 5. Moreover, the thermodynamic database used in TOUGHREACT may also affect the deterministic results.

In deterministic TOUGHREACT simulations, the total dissolved amount of α-quartz is around 0.15 mol, which is difficult to perceive in the y-axis of Figure 6a (green line) due to the scale. One or two orders of magnitude more amounts of chalcedony and α-cristobalite precipitation are observed compared to the muscovite schist scenario (Figures 6c and 6e). H_4SiO_4 is consumed mainly by secondary silica phases and albite-low. The amount of precipitated albite-low is three orders of magnitude greater than the muscovite schist scenario (Figure 6d). This tendency can be accounted for by the larger quartz surface area that increases and eases the interaction between H_4SiO_4 and Na, the most abundant aqueous species in the system. The precipitated calcite amount is four orders smaller than the muscovite schist scenario.

The calculation of the stochastic simulation in MATLAB took a computational time of more than 30 h. In contrast, TOUGHREACT simulation runtimes are between 5 and 20 hours (Hardware specifications: Intel Core i7-12700 CPU @ 2.10 GHz processor with 32 GB of RAM).

4. Cvilica phases and carbonization process are assessed in a metasediment geothermal reservoir during the CO_2-charged fluid injection. Two metasediment rock types, constituted mainly of quartz minerals, are tested to inspect the silica phase and calcite precipitations. The CO_2-fluid-rock geochemical interactions are evaluated at five different injection temperatures with deterministic reactive transport simulator TOUGHREACT and

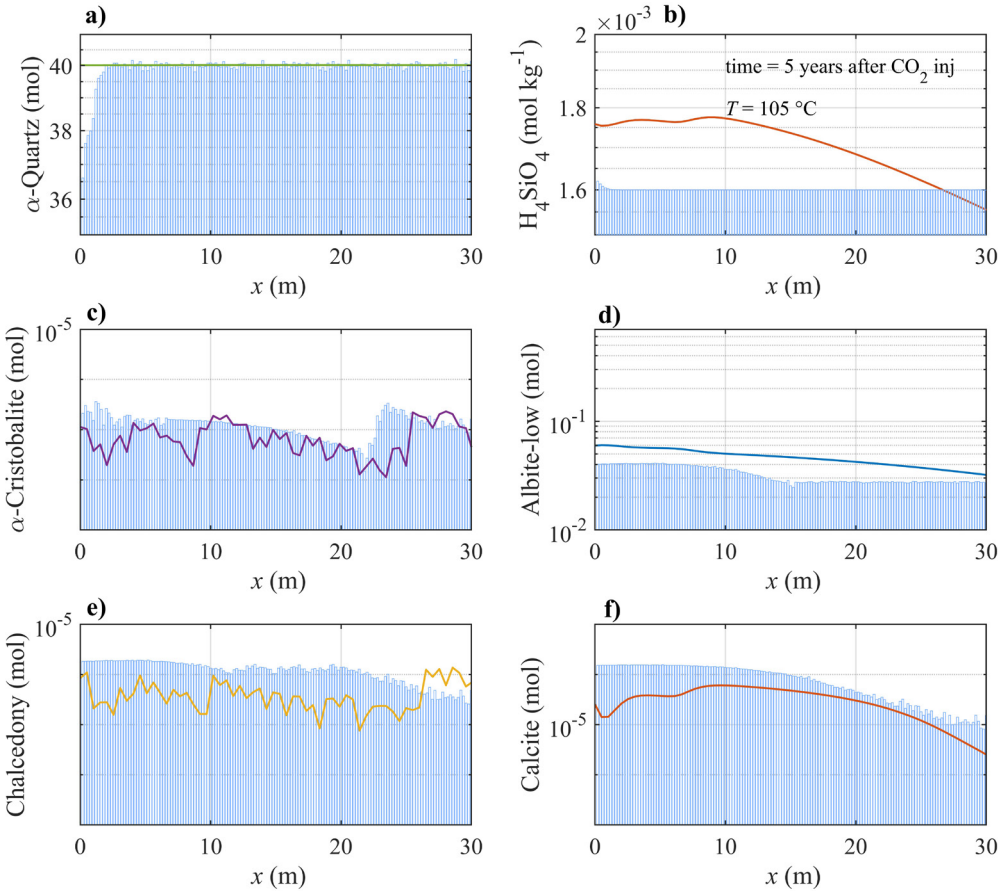


Figure 6. Comparison of stochastic and deterministic reactive transport results of quartz schist scenario over feed zone distance. Temperature is 105 °C in all subplots. Injection takes place on the grid $x = 0$. Bars represent stochastic computation; lines denote the TOUGHREACT simulation results.

compared with Gillespie SSA, providing a precise method for stochastically simulating chemical reaction systems with inherent discreteness and randomness. The advection-diffusion mechanism is taken into account with the back-and-forth jump process, including drift velocity and the jumping rate between compartments.

The Gillespie SSA in this study can be regarded as the exact solution of this chemical system in the reservoir. In contrast, the numerical reactive transport models used to solve sets of coupled PDEs and deterministic reaction rate equations are considered approximate methods because they divide time into infinitesimal time steps. It turns out that the stochastic method can provide a partial validation of the deterministic reactive transport model in this study. The Gillespie SSA outcomes align with the deterministic reactive transport modeling TOUGHREACT results. If the chemical system is fully described, the stochastic method can be used more efficiently where the chemical equilibrium cannot be achieved. However, the computation of a stochastic model is sometimes intense and time-consuming.

The constituents of the rock, salinity, and the pH of the solution are crucial, along with temperature, in the supersaturation process of silica phases and carbonization. During the CO_2-fluid injection process, the CO_2 reacts and precipitates primarily as calcite in the first 10 m distance, and it causes plugging of the flow paths in the muscovite schist scenario. This causes slower fluid flow, lower permeability, and more significant interaction with the host rock minerals, particularly with α-quartz. This interaction reaction contributes more H_4SiO_4 into the system. The H_4SiO_4 is mostly reacted to produce chalcedony, α-cristobalite, and albite-low as secondary minerals.

Regarding geochemical reactions occurring below 120 °C, injecting CO_2 into a layer of quartz schist is more suited. The main reason is the larger volume of the quartz restricting carbonization and plugging the pores. The injection temperature should exceed 105 °C, and the mixing mass fraction of CO_2 should be lower than 0.3% due to the solubility of CO_2 (max. half a tonne of CO_2 can

be mixed with 200 tonnes of effluent fluid per hour). A mass fraction of CO_2 larger than 0.3% is critical to avoid the gaseous phase during injection if the saturation pressure is below 8 MPa at the injection line at 105 °C. Moreover, mixing larger amounts of CO_2 decreases the injection fluid temperature, affecting the silica precipitation.

Acknowledgment
The author thanks Maximillian Berndsen for the fluid and rock sample analysis. Zorlu Energy and Dr Taylan Akın are deeply acknowledged for supplying the fluid and rock samples.

References

Akın S, Orucu Y, Fridriksson T (2020) Characterizing the declining CO2 emissions from turkish geothermal power plants. In: 45th Workshop on Geothermal Reservoir Engineering 10-12 February 2020, Stanford, CA-USA.

Alçiçek H, Varol B, Özkul M (2007). Sedimentary facies, depositional environments and palaeogeographic evolution of the Neogene Denizli Basin, SW Anatolia, Turkey. Sedimentary Geology 202: 596–637. https://doi.org/10.1016/j.sedgeo.2007.06.002

Ancey C, Bohorquez P. Heyman J (2015). Stochastic interpretation of the advection-diffusion equation and its relevance to bed load transport. Journal of Geophysical Research: Earth Surface 120: 2529–2551. https://doi.org/10.1002/2014JF003421

Aradóttir ESP, Sonnethal EL, Björnsson G, Johnsson H (2012). Multidimensional reactive transport modeling of CO2 mineral sequestration in basalts at the Hellisheidi geothermal field, Iceland. International Journal of Greenhouse Gas Control 9: 24-40. https://doi.org/10.1016/j.ijggc.2012.02.006

Bassingthwaighte JB, Butterworth E, Jardine B, Raymond G M (2012). Compartmental modeling in the analysis of biological systems. Computational Toxicology 929: 391–438. https://doi.org/10.1007/978-1-62703-050-2_17

Battistelli A, Calore C, Pruess K (1997). The simulator TOUGH2/EWASG for modelling geothermal reservoirs with brines and non-condensible gas. Geothermics 26 (4): 437–464. https://doi.org/10.1016/S0375-6505(97)00007-2

Berndsen M, Erol S, Akın T, Akın S, Nardini IS et al. (2024). Experimental study and kinetic modeling of high temperature and pressure CO2 mineralisation, International Journal of Greenhouse Gas Control, 132: 104044. https://doi.org/10.1016/j.ijggc.2023.104044

Binning PJ, Celia MA (2008). Pseudokinetics arising from the upscaling of geochemical equilibrium, Water Resources Research, 44: W07410. https://doi.org/10.1029/2007WR006147

Blanc Ph, Lassin A, Piantone P, Azaroual M, Jacquemet N et al. (2012). Thermoddem: a geochemical database focused on low temperature water/rock interactions and waste materials. Applied Geochemistry 27 (10): 2107-2116. https://doi.org/10.1016/j.apgeochem.2012.06.002

Blunt M, Fayers FJ, Orr JFM (1993) Carbon dioxide in enhanced oil recovery, Energy Conversion and Management 34 (9-11): 1197-1204. https://doi.org/10.1016/0196-8904(93)90069-M

Bonafin J, Pietra C, Bonzanini A, Bombarda P (2019). CO2 emissions from geothermal power plants: Evaluation of technical solutions for CO2 reinjection. European Geothermal Congress (EGC) 11-14 The Hague, Netherlands.

Clark DE, Oelkers EH, Gunnarsson I, Sigfússon B, Snæbjörnsdóttir SÓ et al. (2020). CarbFix2: CO2 and H2S mineralization during 3.5 years of continuous injection into basaltic rocks at more than 250 °C. Geochimica et Cosmochimica Acta 279: 45-66. https://doi.org/10.1016/j.gca.2020.03.039

Delerce S, Bénézeth P, Schott J, Oelkers EH (2023). The dissolution rates of naturally altered basalts at pH 3 and 120 °C: implications for the in-situ mineralization of CO2 injected into the subsurface, Chemical Geology 621: 121353. https://doi.org/10.1016/j.chemgeo.2023.121353

DiPippo D (2016). Geothermal Power Plants: Principles, Applications, Case Studies and Environmental Impact. 4th ed. MA, USA: Butterworth-Heinemann. https://doi.org/10.1016/B978-0-08-100879-9.00025-2

Erban R, Chapman J (2020) Stochastic Modelling of Reaction–Diffusion Processes. Cambridge University Press, Cambridge, UK, pp. 307. https://doi.org/10.1017/9781108628389

Erol S, Akın T, Başer A, Saraçoğlu Ö, Akın S (2022a). Geofluid-CO2 injection impact in a geothermal reservoir: evaluation with 3-D reactive transport modeling. Geothermics 98: 102271. https://doi.org/10.1016/j.geothermics.2021.102271

Erol S, Bayer P, Akın T, Akın S (2022b). Advanced workflow for multi-well tracer test analysis in a geothermal reservoir. Geothermics 101: 102375. https://doi.org/10.1016/j.geothermics.2022.102375

Erol S, Akın T, Akın S (2023a). Update for reactive transport modeling of the Kızıldere geothermal field to reduce uncertainties in the early inspections. Turkish Journal of Earth Sciences 32 (4): 541-554. https://doi.org/10.55730/1300-0985.1860

Erol S, Akın T, Akın S (2023b). Monte Carlo model simulations of tracer tests to determine fracture aperture size range in an anisotropic geothermal reservoir. In: 48th Workshop on Geothermal Reservoir Engineering, 6-8 February 2023, Stanford, CA-USA.

Fridriksson T, Mateos A, Orucu Y, Audinet P (2017). Greenhouse gas emissions from geothermal power production. In: 42nd Workshop on Geothermal Reservoir Engineering 13-15 February 2017, Stanford, CA-USA.

Galeczka IM, Stefánsson A, Kleine BI, Gunnarsson-Robin J, Snæbjörnsdóttir SÓ et al. (2022). A pre-injection assessment of CO2 and H2S mineralization reactions at the Nesjavellir (Iceland) geothermal storage site. International Journal of Greenhouse Gas Control 115: 103610. https://doi.org/10.1016/j.ijggc.2022.103610

Gillespie D (1976). A general method for numerically simulating the stochastic time evolution of coupled chemical reactions, Journal of Computational Physics 22: 403–434. https://doi.org/10.1016/0021-9991(76)90041-3

Gillespie D (1977). Exact stochastic simulation of coupled chemical reactions. Journal of Physical Chemistry 81 (25): 2340–2361. https://doi.org/10.1021/j100540a008

Gillespie D (2001). Approximate accelerated stochastic simulation of chemically reacting systems, Journal of Chemical Physics 115 (4): 1716–1733. https://doi.org/10.1063/1.1378322

Griffiths L, Heap MJ, Wang F, Daval D, Gilg HA et al. (2016). Geothermal implications for fracture-filling hydrothermal precipitation, Geothermics, 64: 235–245. https://doi.org/10.1016/j.geothermics.2016.06.006

Gunnarsson I, Arnorsson S (2005). Impact of silica scaling on the efficiency of heat extraction from high-temperature geothermal fluids. Geothermics, 34: 320–329. https://doi.org/10.1016/j.geothermics.2005.02.002

Haizlip JR, Stover MM, Garg SK, Haklidir F, Prina N (2016). Origin and impacts of high concentrations of carbon dioxide in geothermal fluids of western Turkey. In: 41st Workshop on Geothermal Reservoir Engineering, 22-24 February 2016, Stanford, CA-USA.

Heaney PJ (1993). A proposed mechanism for the growth of chalcedony. Contributions to Mineralogy and Petrology 115: 1-66. https://doi.org/10.1007/BF00712979

Huang J, Griffiths DV, Wong SW (2011). Characterizing natural-fracture permeability from mud-loss data, SPE Journal 16 (1): 111-114. https://doi.org/10.2118/139592-PA

Leontidis V, Niknam HP, Durgut I, Taluri L, Manfrida G et al. (2023) Modelling reinjection of two-phase non-condensable gases and water in geothermal wells, Applied Thermal Engineering 223: 120018 https://doi.org/10.1016/j.applthermaleng.2023.120018

Lichtner PC (1996). Chapter 1. Continuum formulation of multicomponent-multiphase reactive transport. In: Reactive Transport in Porous Media. Washington DC, USA: De Gruyter, pp. 1-82. https://doi.org/10.1515/9781501509797-004

Lüttge A, Arvidson RS, Fischer C (2013). A stochastic treatment of crystal dissolution kinetics. Elements 9(3): 183-188. https://doi.org/10.2113/gselements.9.3.183

Matis JH, Wehrly TE (1979). Stochastic models of compartmental systems. Biometrics 35 (1): 199–220. https://doi.org/10.2307/2529945

Molina-Giraldo N, Bayer P, Blum P (2011). Evaluating the influence of thermal dispersion on temperature plumes from geothermal systems using analytical solutions. International Journal of Thermal Sciences 50 (7): 1223–1231. https://doi.org/10.1016/j.ijthermalsci.2011.02.004

Nicholson K (1993). Geothermal Fluids: Chemistry and Exploration Techniques. Berlin, Heidelberg, Germany: Springer. https://doi.org/10.1007/978-3-642-77844-5

Palandri JL, Kharaka YK (2004). A compilation of rate parameters of water-mineral interaction kinetics for application to geochemical modeling. USGS report 2004-1068. U.S. Geological Survey. Menlo Park, CA, USA. https://doi.org/10.3133/ofr20041068

Parkhurst DL, Appelo CAJ (2013). Description of input and examples for PHREEQC version 3 a computer program for speciation, batch-reaction, one-dimensional transport, and inverse geochemical calculations. Amsterdam, the Netherlands: U.S. Geological Survey Techniques and Methods.

Ratouis TMP, Snæbjörnsdóttir SO, Sigfússon B, Gunnarsson I, Voigt MJ et al. (2021). Reactive transport model of CO2 and H2S mineral sequestration at the CarbFix2 reinjection site, Hellisheiði Geothermal Power Plant, SW-Iceland. In: World Geothermal Congress (WGC) October 24-27, Reykjavik, Iceland.

Richter-Feig J, Möckel R, Götze J, Heide G (2018). Investigation of fluids in macrocrystalline and microcrystalline quartz in agate using thermogravimetry-mass-spectrometry. Minerals 8(2): 72. https://doi.org/10.3390/min8020072

Rimstidt JD, Barnes HL (1980). The kinetics of silica-water reactions Geochimica et Cosmochimica Acta 44 (11): 1683-1699. https://doi.org/10.1016/0016-7037(80)90220-3

Risken H (1989) The Fokker–Planck Equation, Methods of Solution and Applications. Berlin, Heidelberg, Germany: Springer, pp. 472. https://doi.org/10.1007/978-3-642-61544-3

Rubin Y (1990). Stochastic modeling of macrodispersion in heterogeneous porous media. Water Resources Research 26 (1): 133–141. https://doi.org/10.1029/WR026i001p00133

Snæbjörnsdóttir SÓ, Sigfússon B, Marieni C, Goldberg D, Gislason SR et al. (2020). Carbon dioxide storage through mineral carbonation. Nature Reviews Earth and Environment 1: 90–102. https://doi.org/10.1038/s43017-019-0011-8

Stundzia AB, Lumsden CJ (1996) Stochastic simulation of coupled reaction–diffusion processes. Journal of Computational Physics 127 (1): 196-207. https://doi.org/10.1006/jcph.1996.0168

Thakur AK, Reseigno A, Sehafer DE (1972). On the stochastic theory of compartments: I. a single compartment system. The Bulletin of Mathematical Biophysics 34: 53–63. https://doi.org/10.1007/BF02477024

Van den Heuvel DB, Gunnlaugsson E, Gunnarsson I, Stawski TM, Peacock CL et al. (2018). Understanding amorphous silica scaling under well-constrained conditions inside geothermal pipelines. Geothermics, 76: 231-241. https://doi.org/10.1016/j.geothermics.2018.07.006

Wang X, Alvarado V, Swoboda-Colberg N, Kaszuba PJ (2013). Reactivity of dolomite in water-saturated supercritical carbon dioxide: significance for carbon capture and storage and for enhanced oil and gas recovery, Energy Conversion and Management 65: 564-573. https://doi.org/10.1016/j.enconman.2012.07.024

Whitney DL, Evans BW (2010). Abbreviations for names of rock-forming minerals. American Mineralogist, 95 (1): 185-187. https://doi.org/10.2138/am.2010.3371

Xu T, Sonnenthal E, Spycher N, Pruess K (2008). TOUGHREACT User's Guide: A Simulation Program for Non-isothermal Multiphase Reactive Transport in Variably Saturated Geologic Media, version 1.2.1. Report LBNL-55460-2008., Lawrence Berkeley National Laboratory. Berkeley, CA, USA.